

Improving Room-Temperature Li-Metal Battery Performance by In Situ Creation of Fast Li⁺ Transport Pathways in a Polymer-Ceramic Electrolyte

Jing Yu, Guodong Zhou, Yueqing Li, Yuhao Wang, Dengjie Chen, and Francesco Ciucci*

Composite polymer-ceramic electrolytes have shown considerable potential for high-energy-density Li-metal batteries as they combine the benefits of both polymers and ceramics. However, low ionic conductivity and poor contact with electrodes limit their practical usage. In this study, a highly conductive and stable composite electrolyte with a high ceramic loading is developed for high-energy-density Li-metal batteries. The electrolyte, produced through in situ polymerization and composed of a polymer called poly-1,3-dioxolane in a poly(vinylidene fluoride)/ceramic matrix, exhibits excellent room-temperature ionic conductivity of 1.2 mS cm⁻¹ and high stability with Li metal over 1500 h. When tested in a Li|electrolyte|LiFePO₄ battery, the electrolyte delivers excellent cycling performance and rate capability at room temperature, with a discharge capacity of 137 mAh g⁻¹ over 500 cycles at 1 C. Furthermore, the electrolyte not only exhibits a high Li⁺ transference number of 0.76 but also significantly lowers contact resistance (from 157.8 to 2.1 Ω) relative to electrodes. When used in a battery with a high-voltage LiNi_{0.8}Mn_{0.1}Co_{0.1}O₂ cathode, a discharge capacity of 140 mAh g⁻¹ is achieved. These results show the potential of composite polymer-ceramic electrolytes in room-temperature solid-state Li-metal batteries and provide a strategy for designing highly conductive polymer-in-ceramic electrolytes with electrode-compatible interfaces.

reduction potential (−3.04 V vs the standard hydrogen electrode).^[1] However, Li-metal anodes (LMAs) are highly reactive with commercial organic liquid electrolytes, leading to electrolyte decomposition and reduced battery cycle life.^[2] Moreover, if a liquid electrolyte is used, Li dendrites form easily during cycling. In turn, these dendrites may penetrate commercial separators and cause internal short circuits.^[2b,3] In addition, commercial organic liquids are flammable, severely compromising battery safety.^[2b,3] Substituting flammable organic liquid electrolytes with a solid-state electrolyte that is stable against LMAs overcomes these critical issues.

Among solid-state electrolytes, composite polymer-ceramic electrolytes (CPEs) have shown considerable promise for Li-metal batteries to boost energy density and safety.^[4] The ceramics in CPEs enhance ionic conductivity due to the increased amorphization of the polymer host, while the polymers offer excellent processability and flexibility, ensuring good interfacial contact, and easy fabrication.^[4b]

A variety of ceramic fillers (e.g., SiO₂, TiO₂, Li₇La₃Zr₂O₁₂, and Li₁₀GeP₂S₁₂)^[5] and polymers (e.g., poly(ethylene oxide) (PEO), poly(vinylidene fluoride) (PVDF), poly(vinylidene fluoride-co-hexafluoropropylene), and polyacrylonitrile (PAN)) have been used in CPEs.^[5b,6] In general, a higher ionic conductivity of a CPE is achieved at lower ceramic filler

1. Introduction

Lithium metal is widely regarded as an ideal anode material for next-generation rechargeable batteries due to its high theoretical specific capacity (3860 mAh g⁻¹) and low electrochemical

J. Yu
Department of Chemistry and Chemical Engineering
Zhongkai University of Agriculture and Engineering
Guangzhou 510225, China

J. Yu, G. Zhou, Y. Wang, F. Ciucci
Department of Mechanical and Aerospace Engineering
The Hong Kong University of Science and Technology
Hong Kong 000000, China
E-mail: francesco.ciucci@uni-bayreuth.de, mefrank@ust.hk

Y. Li, D. Chen
College of Chemistry and Materials Science
Jinan University
Guangzhou 510632, China

F. Ciucci
Chair of Electrode Design for Electrochemical Energy Systems
University of Bayreuth
95447 Bayreuth, Bavaria, Germany
F. Ciucci
Bavarian Center for Battery Technology (BayBatt)
95447 Bayreuth, Bavaria, Germany

 The ORCID identification number(s) for the author(s) of this article can be found under <https://doi.org/10.1002/smll.202302691>

© 2023 The Authors. Small published by Wiley-VCH GmbH. This is an open access article under the terms of the Creative Commons Attribution License, which permits use, distribution and reproduction in any medium, provided the original work is properly cited.

DOI: 10.1002/smll.202302691

concentrations.^[5b,7] Increasing the content of ceramic particles can improve the mechanical strength and safety of a CPE, but may also reduce its flexibility.^[4b,8] Consequently, the ceramic filler loading in CPEs is usually kept low. In turn, ceramic particles are isolated and unable to form a continuous network for Li⁺ transport. This can limit the performance of CPEs in Li-metal batteries.^[4b,8b,9]

Recently, Zheng et al. studied Li⁺ transport mechanisms in a Li₇La₃Zr₂O₁₂-PEO (LiClO₄) composite electrolyte with 50 wt.% of Li₇La₃Zr₂O₁₂ using Li nuclear magnetic resonance.^[10] The authors found that Li⁺ transport occurred primarily in the Li₇La₃Zr₂O₁₂ phase in the composite electrolyte.^[10] Following this important work, the development of composite electrolytes with high ceramic loading has emerged.^[11] For instance, the Goodenough group proposed a polymer-in-ceramic (PIC) electrolyte containing Li_{6.4}La₃Zr_{1.4}Ta_{0.6}O₁₂ (LLZTO), lithium bis(trifluoromethanesulfonyl)imide (LiTFSI), and PEO.^[6a] When tested in a Li symmetric cell, this PIC electrolyte was able to prevent dendrite formation for 680 h.^[6a] However, even with a high loading of 60 wt.% of LiTFSI in the PEO/LLZTO-based PIC electrolyte, its ionic conductivity was only able to reach 10⁻⁴ S cm⁻¹ at 55 °C.^[6a] The poor interparticle contact between the ceramic and polymer in PIC blocked the Li⁺ transport, thus reducing ionic conductivity.^[6a,12] While various approaches, including adjusting the ceramic particle size^[13] and morphology,^[14] have been investigated to address this issue, it has proven difficult to effectively improve interparticle Li⁺ transport in PICs. As a result, the ionic conductivity of PICs at room temperature has not achieved the desired level of performance.

Another major challenge with PIC electrolytes is the high interfacial resistance caused by poor surface contact between the electrolyte and electrode.^[13a,15] This poor contact is more severe for PICs with high ceramic content, which increases electrolyte rigidity and reduces wettability with electrodes. On the LMA side, poor interfacial contact leads to current density non-uniformities, which trigger the formation of Li dendrites and “dead” Li. “Dead” Li reacts with the electrolyte during cycling, increasing the thickness of the solid electrolyte interface (SEI) and hindering battery performance.^[11b,16] On the cathode side, poor interfacial contact can also increase impedance and negatively impact battery performance.^[5e,17] Additionally, the electrochemical instability between the electrolyte and cathode and the volumetric changes in the active cathode material during cycling contribute to an increase in charge transfer resistance originating from the electrolyte/cathode interface, leading to high polarizations, low active material utilization, and reduced battery performance.^[18] The use of a soft polymer-based buffer layer between the electrolyte and electrode can improve PIC interfacial resistance.^[4b,19] For example, Huo et al. designed a multi-layer electrolyte consisting of a PIC electrolyte (80 vol.% LLZTO in PEO) sandwiched between two flexible ceramic-in-polymer (20 vol.% LLZTO in PEO) electrolytes.^[13a] Thanks to the presence of the two buffer layers, this battery achieved a discharge capacity of 118.6 mAh g⁻¹ at 0.1 C and room temperature.^[13a] In other research, Chen et al. directly cast a LLZTO@PAN composite electrolyte on the cathode surface and added a thin PEO/LiTFSI electrolyte layer between LMA and the electrolyte.^[9] The PEO/LiTFSI layer reduced interfacial resistance and prevented chemical reactions between LLZTO@PAN and LMA from occurring.^[9] A cor-

responding LLZTO@PAN|PEO-based Li/LiFePO₄ (LFP) battery delivered an initial discharge capacity of 167 mAh g⁻¹ at 0.1 C and 60 °C with a capacity retention of 89.6% over 100 cycles.^[9] Despite the improved performance, the multilayer structure complicates electrolyte preparation, thus hindering process scalability. Furthermore, introducing inactive materials into a battery reduces its energy density. In short, the development of PICs with small interfacial resistance has proven to be a considerable challenge. In situ polymerization processes have received significant attention as a means of improving the interface between the electrolyte and electrode in solid polymer electrolytes for Li-metal batteries.^[20] These processes are commonly based on thermal or photo-curing methods, but can be limited in terms of scalability. In contrast, we have developed an in situ polymerization approach based on ring-opening polymerization at room temperature that avoids damaging the battery and is more suitable for large-scale production.

This work focuses on developing a novel approach for the in situ polymerization of poly-PICs, a class of highly conductive, dendrite-free, and safe PIC electrolytes enhanced with poly-1,3-dioxolane (polyDOL). By injecting polyDOL into a PVDF/LLZTO-based PIC scaffold and spontaneously polymerizing the entire assembly at room temperature, higher ionic conductivity and enhanced interfacial contacts were obtained, leading to the successful creation of an integrated electrode/electrolyte. The use of a PIC scaffold ensures the mechanical strength and compatibility of the electrolyte with electrodes, while the incorporation of polyDOL improves interfacial contact and ionic conductivity due to its ability to wet the PVDF/LLZTO composite. This combination allows for the successful development of an integrated electrode/electrolyte. As a result, the best poly-PIC electrolyte among those developed, i.e., poly-PIC with 80 wt.% LLZTO (poly-PIC80), exhibited: 1) high ionic conductivity (0.6, 1.3, and 2.1 mS cm⁻¹ at 0, 30, and 60 °C, respectively); 2) a high Li⁺ transference number (0.76); and 3) a wide electrochemical window (≈4.83 V vs Li/Li⁺). Moreover, the integrated electrolyte/electrode formed through in situ polymerization ensures the formation of gapless electrolyte/electrode interfaces with reduced interfacial resistances (from 157.8 to 2.1 Ω). These efforts have led to the development of high-energy-density, room-temperature solid-state Li-metal batteries. For instance, a Li|poly-PIC80|Li cell demonstrated excellent stripping and plating at 0.2 mA cm⁻² over 1500 h. The Li|poly-PIC80|LFP battery delivered excellent room-temperature cycling stability for >500 cycles with a discharge capacity of 137 mAh g⁻¹ at 1 C and an exceptional rate capability of 126 mAh g⁻¹ at 3 C. As the polyDOL precursor effectively wetted the porous electrode layer before polymerization, cathodes with higher mass loading could be used. Remarkably, LiNi_{0.8}Mn_{0.1}Co_{0.1}O₂ (NMC811) with a mass loading of 6.9 mg cm⁻² was assembled into a Li|poly-PIC80|NMC811 battery, which had a high discharge capacity of 140 mAh g⁻¹ at 0.1 C for >80 cycles at room temperature. In conclusion, the use of a poly-PIC electrolyte made through in situ polymerization represents an effective approach for the development of PIC electrolytes with high ionic conductivity and low interfacial resistances. This has the potential to create safe and high-energy-density solid-state Li-metal batteries that can operate at room temperature, offering a promising solution for the next-generation of rechargeable batteries.

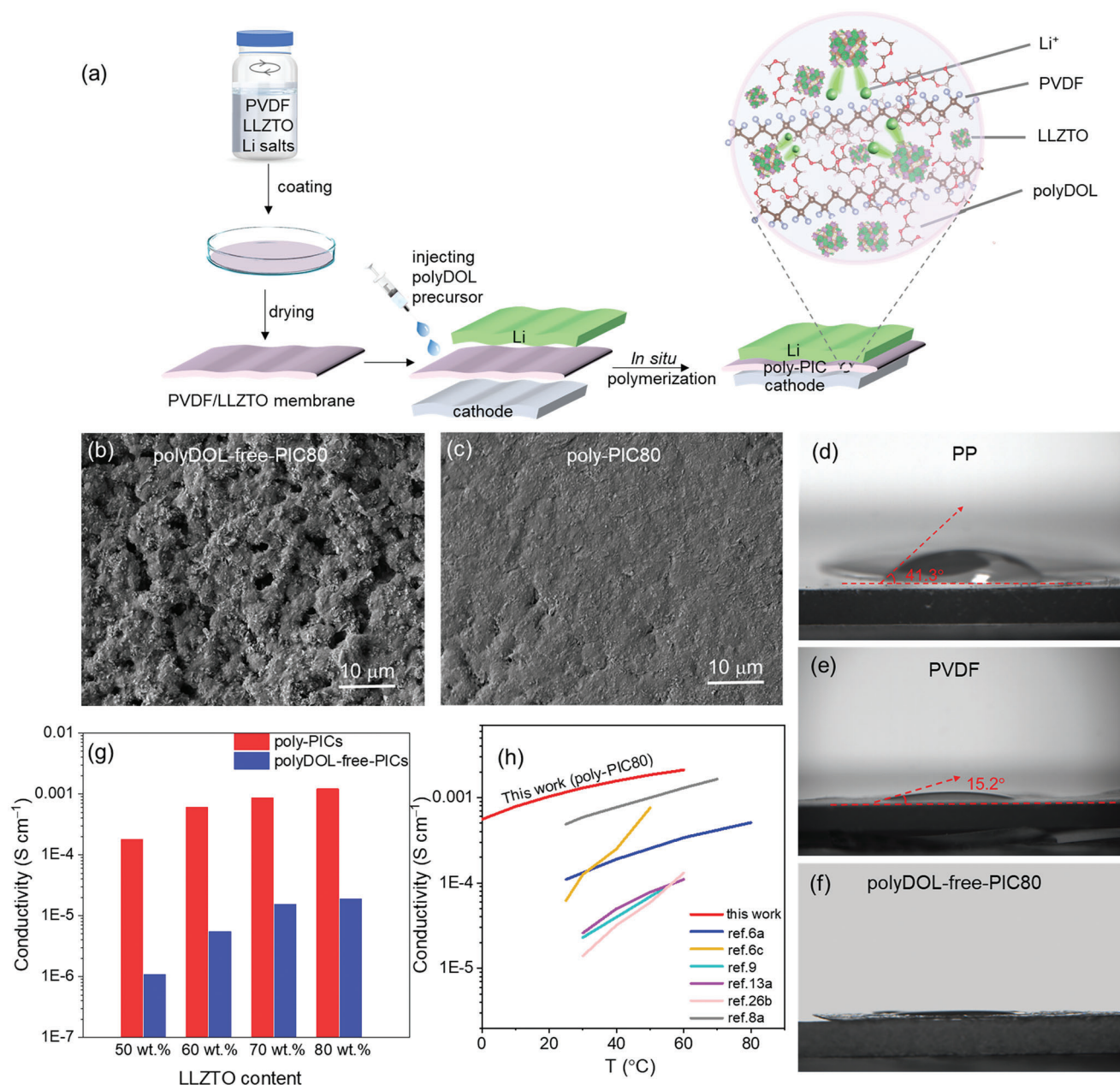


Figure 1. a) Schematic illustrating the preparation of a poly-PIC-based battery. Surface SEM images of b) polyDOL-free-PIC80 and c) poly-PIC80. Contact angles between polyDOL and d) a PP separator, e) a PVDF membrane, and f) the polyDOL-free-PIC membrane. g) Ionic conductivity of polyDOL-free-PICs and poly-PICs at room temperature. h) Ionic conductivity of poly-PIC80 versus temperature compared against previously reported PIC electrolytes.

2. Results and Discussion

The poly-PIC was facilely prepared by injecting polyDOL into the PVDF/LLZTO membrane (i.e., a mixture of LiTFSI/LiBOB dual-salt, PVDF, and LLZTO). The LiTFSI/LiBOB dual-salt recipe was chosen based on our previous work,^[21] and PVDF/LLZTO were used to construct the polymer-ceramic composite electrolyte. **Figure 1a** shows schematically the poly-PIC-based battery preparation. A free-standing PVDF/LLZTO membrane was produced by first film coating followed by drying at 60 °C in a vacuum oven. The polyDOL, which was prepared as described below, was then

incorporated into the PVDF/LLZTO-based battery and polymerized in situ at room temperature. The polyDOL was fabricated by mixing the DOL monomer with LiTFSI, methyl propionate (MP), fluoroethylene carbonate (FEC), and LiPF₆ (more details are in the Experimental Section). As shown in Movie S1 and Figure S1a (Supporting Information), the produced polyDOL is a transparent, solid-state analogue. Figure S1b (Supporting Information) reports the Fourier-transform infrared (FTIR) spectra of DOL and polyDOL. Different from the DOL spectrum, polyDOL's FTIR had a prominent long-chain vibration peak at 845 cm⁻¹ originating from the ring-opening polymerization of DOL.^[20a,22]

Garnet LLZTO powders (Figure S2a, Supporting Information) with an average particle diameter of 562 nm (Figure S2b, Supporting Information) were prepared using a solid-state reaction following our previous works.^[6b,23] The sintered LLZTO pellet delivered a total ionic conductivity of 0.2 mS cm^{-1} at room temperature (Figure S2c, Supporting Information), consistent with the literature^[24] and our previous research^[23,25] Figure S2d (Supporting Information) presents the X-ray diffraction (XRD) patterns of the LLZTO powder and poly-PIC (e.g., poly-PIC80). LLZTO had a pure cubic peak structure without detectable impurities, suggesting the successful synthesis of LLZTO. The poly-PIC80 electrolyte displayed identical peaks as those of LLZTO, implying that LLZTO was structurally stable during poly-PIC preparation. Surface images of the pristine polyDOL-free-PIC80 (PIC with 80 wt.% LLZTO) and poly-PIC80 are shown in Figure 1b,c. The surface of polyDOL-PIC80 was smoother and denser than that of polyDOL-free-PIC80, suggesting that polyDOL percolated into the polyDOL-free-PIC80 bulk. Figure S3a,b (Supporting Information) shows that both the polyDOL-free-PIC80 and poly-PIC80 electrolytes had similar thicknesses of $\approx 105 \mu\text{m}$. Contact angle experiments demonstrated the good wettability of polyDOL against the polyDOL-free-PIC80. The contact angles of the polyDOL precursor in contact with a PP separator (celgard@2500), a PVDF membrane, and polyDOL-free-PIC80 were 41.3° , 15.2° , and $\approx 0^\circ$, respectively (Figure 1d–f), where lower contact angles imply better wettability.

Figure 1g presents the room-temperature ionic conductivity of the polyDOL-free-PICs and poly-PICs for various LLZTO ratios. All poly-PICs had higher ionic conductivity than polyDOL-free-PICs. For example, the ionic conductivity of poly-PIC80 was 1.2 mS cm^{-1} at room temperature, a value two orders of magnitude higher than that of polyDOL-free-PIC80 ($1.8 \times 10^{-2} \text{ mS cm}^{-1}$). Furthermore, the room-temperature ionic conductivity of all polyDOL-free-PICs and poly-PICs increased by nearly an order of magnitude as the LLZTO content increased from 50 to 80 wt.%, confirming the positive impact of this ceramic on the ionic conductivity.^[26] Free-standing poly-PIC50, poly-PIC60, poly-PIC70, and poly-PIC80 membranes were obtained as shown in digital images (Figure S4a–d, Supporting Information). However, when the LLZTO content was 90 wt.%, a free-standing membrane could not be obtained (Figure S4e, Supporting Information).

The ionic conductivity of the poly-PIC membranes was measured as a function of temperature (Figure S5a, Supporting Information). Among the poly-PICs, poly-PIC80 had the highest ionic conductivity at all investigated temperatures. For instance, the ionic conductivity of poly-PIC80 was 0.6, 1.3, and 2.1 mS cm^{-1} at 0, 30, and 60°C , respectively, much higher than other recently reported PIC electrolytes (Figure 1h)^[6a,c,8a,9,13a,26b] For the poly-PICs, the activation energy obtained by fitting the conductivity against temperature using the Arrhenius equation decreased with increasing LLZTO content (Figure S5b and Table S1, Supporting Information), further indicating that increasing ceramic content promoted Li^+ transport. In particular, poly-PIC80 had the lowest activation energy (E_a) of 0.17 eV among the studied poly-PICs, lower than previously reported PIC electrolytes.^[8a,9,26] Figure S6 (Supporting Information) schematically illustrates possible Li^+ transport pathways in the polyDOL-free-PIC and poly-PIC electrolyte. Specifically, due to polyDOL's excellent wettability

against the polyDOL-free-PIC scaffold (Figure 1f), polyDOL penetrated the polyDOL-free-PIC bulk, increasing the fraction of the material within that Li^+ conduction could occur. In addition, in situ fabrication enabled a closely integrated electrode/electrolyte assembly, which improved interfacial contact, thus reducing interfacial resistance. As shown in Figure S7a (Supporting Information), the in situ fabricated poly-PIC80 had good interfacial contact with the Li metal anode, exhibiting a nearly seamless connection. In contrast, visible gaps were observed between the polyDOL-free-PIC80 and Li metal (Figure S7b, Supporting Information). Furthermore, the total resistance decreased after the addition of polyDOL (Figure S8 and Table S3, Supporting Information). For example, the interfacial resistance (R_{int}) of the poly-PIC80-based battery ($\approx 2.1 \Omega$) was nearly two orders of magnitude lower than that of the polyDOL-free-PIC80-based battery ($\approx 157.8 \Omega$). Notably, thanks to the formation of an integrated structure after adding polyDOL, the poly-PIC80-based Li/LFP battery presented a much smaller charge transfer resistance (R_{ct}) ($\approx 99.0 \Omega$) than the polyDOL-free-PIC80-based Li/LFP battery ($\approx 2420.0 \Omega$).

Li^+ transference number, t_{Li^+} , is a vital parameter for an electrolyte and generally it is sought to be close to one. As shown in Figure 2a–d, the t_{Li^+} of poly-PICs increased from 0.32 to 0.76 with increasing LLZTO content, as $t_{\text{Li}^+} = 1$ for LLZTO.^[17] The t_{Li^+} of poly-PIC70 and poly-PIC80 were 0.73 and 0.76, respectively, much higher than the value of typical polymer (<0.5) and liquid (0.2–0.3) electrolytes.^[27] A high t_{Li^+} has been reported to reduce the concentration polarization within the electrolyte and promote a uniform Li^+ deposition, in turn preventing Li dendrite formation.^[4b,28] Besides Li^+ transport, the mechanical strength and thermal properties of poly-PICs were tested by tensile tests and thermogravimetric analysis (TGA). The increased proportion of LLZTO in poly-PICs improved mechanical strength. As shown in Figure 2e, poly-PIC80 had the highest Young's modulus of 117.7 MPa among poly-PICs. The thermal stability of poly-PICs also improved with increasing LLZTO content (Figure 2f).

The compatibility between LMA and electrolyte is critical to achieving high capacity and long-cycle stability. As shown in Figure 3a,b, the Li|poly-PIC50|Li and Li|poly-PIC60|Li symmetric cells were cycled at 0.2 mA cm^{-2} and 0.2 mAh cm^{-2} at 23°C . The polarization increased during cycling and the poly-PIC50 and poly-PIC60 cells short-circuited at 747 and 904 h, respectively. In sharp contrast, the symmetric cells with poly-PIC70 and poly-PIC80 could cycle stably for 1500 h under identical conditions. Furthermore, poly-PIC80 had the lowest voltage response among all poly-PICs. Li/Cu cells were assembled to further evaluate the compatibility between the poly-PICs and the LMA. As shown in Figure S9a,b (Supporting Information), with the continuous Li plating/stripping, polarization resistances gradually increased for the Li|poly-PIC50|Cu and Li|poly-PIC60|Cu cells. In addition, the Coulombic efficiency (CE) of both cells declined to 56% and 60% after the 290th and 296th cycles (Figure 3c), respectively. In contrast, the Li|poly-PIC70|Cu and Li|poly-PIC80|Cu cells displayed outstanding cycling stability over 350 cycles with an average CE of $\approx 95\%$ (Figure 3c). The Li|poly-PIC80|Cu cell had a lower polarization voltage than Li|poly-PIC70|Cu. For instance, at the 350th cycle, the polarization voltage of Li|poly-PIC80|Cu was 46 mV, less than half that of Li|poly-PIC70|Cu (106 mV), suggesting that poly-PIC80 had better compatibility with LMA than

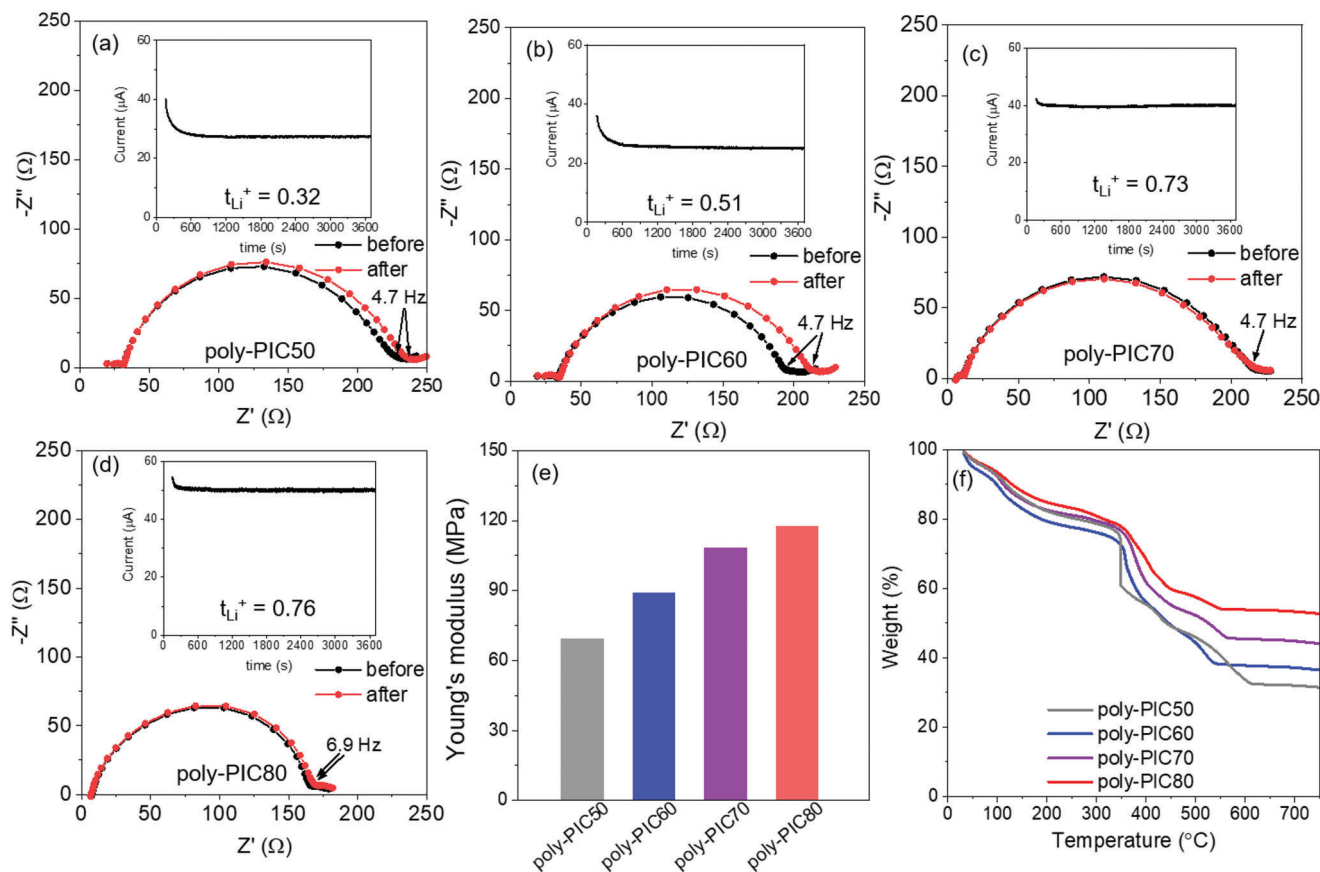


Figure 2. Li transference number, t_{Li^+} , of a) poly-PIC50, b) poly-PIC60, c) poly-PIC70, and d) poly-PIC80 at room temperature. e) Young's modulus and f) TG curves of poly-PICs.

all other prepared electrolytes (Figure S9c,d, Supporting Information). Linear sweep voltammetry was used to study the electrochemical window of poly-PICs. As shown in Figure 3d, all the poly-PICs prepared had an electrochemical window >4.5 V versus Li/Li⁺. Furthermore, the electrochemical window widened as the LLZTO content increased. As shown in Figure 3d and Table S1 (Supporting Information), the oxidation for poly-PIC80 started at ≈ 4.83 V, whereas for poly-PIC50 it was ≈ 4.67 V.

To evaluate the electrochemical performance of poly-PICs, Li/LFP batteries were assembled and operated between 2.5 and 4.2 V. As shown in Figure 4a,b and Figure S10a (Supporting Information), Li|poly-PIC50|LFP had a much lower capacity compared with other poly-PICs-based Li/LFP batteries, mainly due to the lower ionic conductivity of poly-PIC50. The poly-PIC60-based battery showed fluctuating CE and experienced significant capacity decay after just 320 cycles, stopping operation at the 367th cycle (Figure 4a; Figure S10b, Supporting Information). In contrast, both poly-PIC70 and poly-PIC80-based Li/LFP batteries delivered stable cycling performance with retained discharge capacities of ≈ 137 mAh g⁻¹ at the 500th cycle and high CEs of 99.9% over 500 cycles at 23 °C and 1 C (Figure 4a; Figure S10c,d, Supporting Information). Moreover, Li|poly-PIC70|LFP and Li|poly-PIC80|LFP batteries showed excellent rate capability at higher C-rates (Figure 4c; Figure S11, Supporting Information). For instance, Li|poly-PIC80|LFP delivered specific capacities of 164, 156, 145, 135, and

126 mAh g⁻¹ at 0.2, 0.5, 1, 2, and 3 C, respectively (Figure 4c). When the current density returned to 1 C, the specific capacity recovered to 145 mAh g⁻¹ and the cell could be operated stably for 50 cycles (Figure S11c, Supporting Information). The Li|polyDOL-free-PIC80|LFP battery was also tested for comparison. As shown in Figure S12a (Supporting Information), the polyDOL-free-PIC80-based battery had a low initial CE of 20.7% with a specific capacity of 4 mAh g⁻¹ at 0.2 C at room temperature. The poly-PIC80-based battery had a significantly better capacity of 158 mAh g⁻¹ with an initial CE of 95.2%, see Figure S12b (Supporting Information). As the mass loading of LFP increased to 7.9 mg cm⁻², the Li|poly-PIC80|LFP battery delivered a high initial CE of 98.4% and sustained a discharge capacity of 150 mAh g⁻¹ over 50 cycles at 23 °C and 0.1 C (Figure S13, Supporting Information).

A high-energy Li-metal battery with a high-voltage NMC811 cathode (mass loading of 6.9 mg cm⁻²) and poly-PIC80 as the electrolyte was prepared. As shown in Figure 4d,e, this Li|poly-PIC80|NMC811 battery operated from 2.8 to 4.3 V and maintained a discharge capacity of 140 mAh g⁻¹ over 80 cycles at 0.1 C. The poly-PIC80-based battery outperformed recently reported PIC-based batteries (Table S2, Supporting Information). Furthermore, a flexible and safe poly-PIC80-based pouch cell was constructed. As shown in Figure S14 (Supporting Information), a Li|poly-PIC80|LFP pouch cell illuminated a red light-emitting

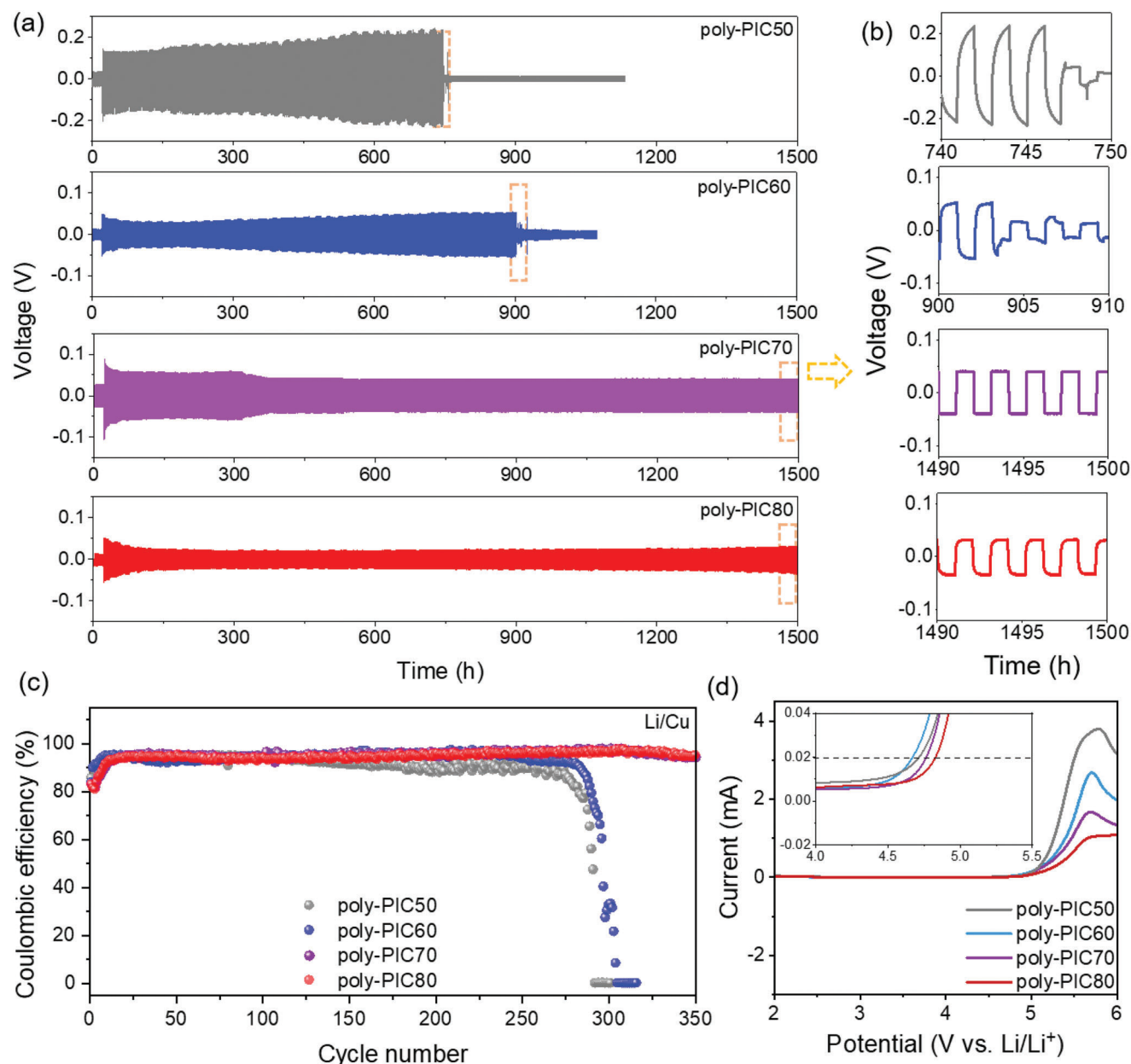


Figure 3. a) Li plating/stripping behavior and b) enlarged voltage profiles of poly-PICs. c) Cycling performance of the Li|poly-PIC|Cu cells. d) Linear sweep voltammograms of the Li|poly-PIC|SS (SS = stainless steel) cells.

diode (LED) when bent, cut, or folded. Moreover, the cut pouch cell was functional even under flame exposure (Figure S14b and Movie S2, Supporting Information).

To elucidate the mechanisms underlying the stable cycling performance of the poly-PIC80-based Li-metal batteries, further characterizations were conducted. Scanning electron microscopy (SEM) and X-ray photoelectron spectroscopy (XPS) were used to analyze the LMA surfaces after the rate performance tests. These rate performance tests, consisting of five cycles at 0.2, 0.5, 1, 2, and 3 C, followed by an additional 25 cycles at 1 C were carried out for all the Li|poly-PIC|LFP batteries prepared. As shown in Figure 5a,b, surface protrusions and Li dendrites were ob-

served on LMA@poly-PIC50 (LMA from the Li|poly-PIC50|LFP cell) and LMA@poly-PIC60 (LMA from the Li|poly-PIC60|LFP cell). Whereas the LLZTO content increased, SEM images of LMA@poly-PIC70 and LMA@poly-PIC80 (Figure 5c,d) indicated more uniform and smoother surfaces, suggesting suppressed dendrite growth. The surfaces of the cycled LMAs were then characterized by XPS depth profiling (Figure 5e). With reference to the C 1s spectra, all the LMAs surfaces showed the hydrocarbon (C–C/C–H, 284.8 eV), polyether carbon (C–O, 286.6 eV), carbonyl group (C=O, 288.8 eV), and Li carbonate (CO₃, 289.9 eV) peaks.^[29] The significant C–F (293.0 eV) peak in LMA@poly-PIC50 was mainly due to LiTFSI decomposition during cycling.

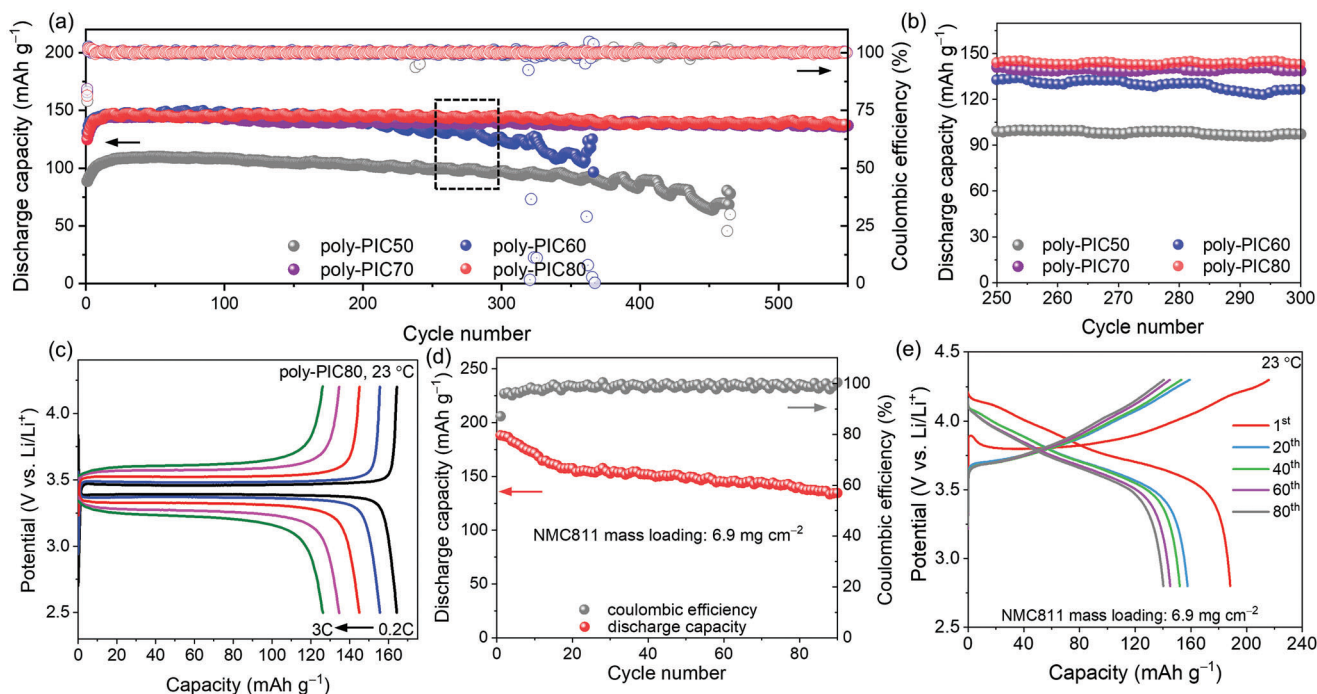


Figure 4. a) Cycling stability and b) enlarged cyclic profiles from 250 to 300 cycles of Li/LFP batteries with poly-PICs at 23 °C and 1 C. c) Typical charge–discharge curves of Li|poly-PIC|LFP batteries at various C-rates. d) Cycling performance and e) typical charge–discharge curves of Li|poly-PIC80|NMC811 batteries with a mass loading of 6.9 mg cm⁻² of NMC811 within the cathode.

As the LLZTO content increased, the C–F peak intensity reduced with C–F peak being barely observable for poly-PIC80, indicating inhibited LiTFSI decomposition. Similar considerations can be made from the analysis of the F 1s spectra. The C–F₃ (688.5 eV) peak was more prominent for LMA@poly-PIC50 than for LMA@poly-PIC60, LMA@poly-PIC70, and LMA@poly-PIC80. Indeed, the peak area ratio of LiF to the total area of CF_x, BF, and LiF (48% of LMA@poly-PIC60, 51% of LMA@poly-PIC70, and 52% of LMA@poly-PIC80) increased, suggesting the formation of a stable SEI layer. After sputtering, these differences could no longer be detected, with LiF being the dominant peak of the inner part of the SEI. Furthermore, the presence of peaks attributable to B–F (686.8 eV) in the F 1s spectra and B–O and B–F peaks in the B 1s spectra (Figure S15, Supporting Information) originating from the decomposition of LiBOB, suggests that LiBOB was also involved in the formation of the SEI on LMA@poly-PIC80.

Density functional theory (DFT) calculations were carried out to elucidate the SEI formation mechanism. The lowest unoccupied molecular orbital (LUMO) was calculated for each electrolyte component. A low LUMO energy indicates a high tendency of species to be reduced. As shown in Figure 6a, LiBOB had a low LUMO energy of –3.16 eV, much lower than LiTFSI (–1.63 eV), indicating that LiBOB facilitates SEI formation, consistent with the XPS results. Furthermore, polyDOL had the highest LUMO energy of 0.94 eV among the investigated components, suggesting that polyDOL is stable against LMA. Therefore, adding polyDOL to the electrolyte can improve its stability with LMA. The impact of polyDOL addition was further investigated by molecu-

lar dynamics (MD) simulations of the PVDF-based polymer electrolyte and polyDOL-based polymer electrolyte (see snapshots in Figure 6b,c). Figure 6d shows the mean square displacement (MSD) of Li⁺, TFSI⁻, and PVDF in the PVDF-based polymer electrolyte. The diffusion coefficients (Figure 6e) were calculated by regressing the MSD curves against time (see details in the computational section). Species in the polyDOL-based polymer electrolyte showed higher diffusion coefficients. For instance, the diffusion coefficient of Li⁺ at room temperature was improved to 7.04 × 10⁻¹³ m² s⁻¹, higher than that in the PVDF-based electrolyte (3.62 × 10⁻¹³ m² s⁻¹) (Figure 6e). The radial distribution functions, g(r), of TFSI⁻ anion and polyDOL molecule with respect to Li⁺ were calculated to analyze the Li⁺ solvation structure (Figure S16a, Supporting Information). A sharp peak of TFSI⁻ was observed at 2.0 Å, indicating its presence in the first solvation shell of Li⁺. The coordination number (CN) at a distance r from the referenced Li⁺ was obtained by integrating g(r) from 0 to r. The value of CN of a certain species indicated its placement in the Li⁺ solvation shell. As shown in Figure S16b (Supporting Information), the CN number confirms that Li⁺ are close to TFSI⁻ with a high CN of 1.54 at 3.0 Å, indicating that the TFSI⁻ anion enters the first Li⁺ solvation shell. This structure is comparable to that seen in localized concentrated electrolytes, which has been shown to promote Li⁺ transport and electrochemical stability.^[22a,30] Therefore, incorporating the in situ generated polyDOL-based polymer electrolyte greatly promotes the Li⁺ transport. As a result, poly-PIC electrolytes have higher ionic conductivity than polyDOL-free-PIC electrolytes with the same ceramic content (Figure 1g).

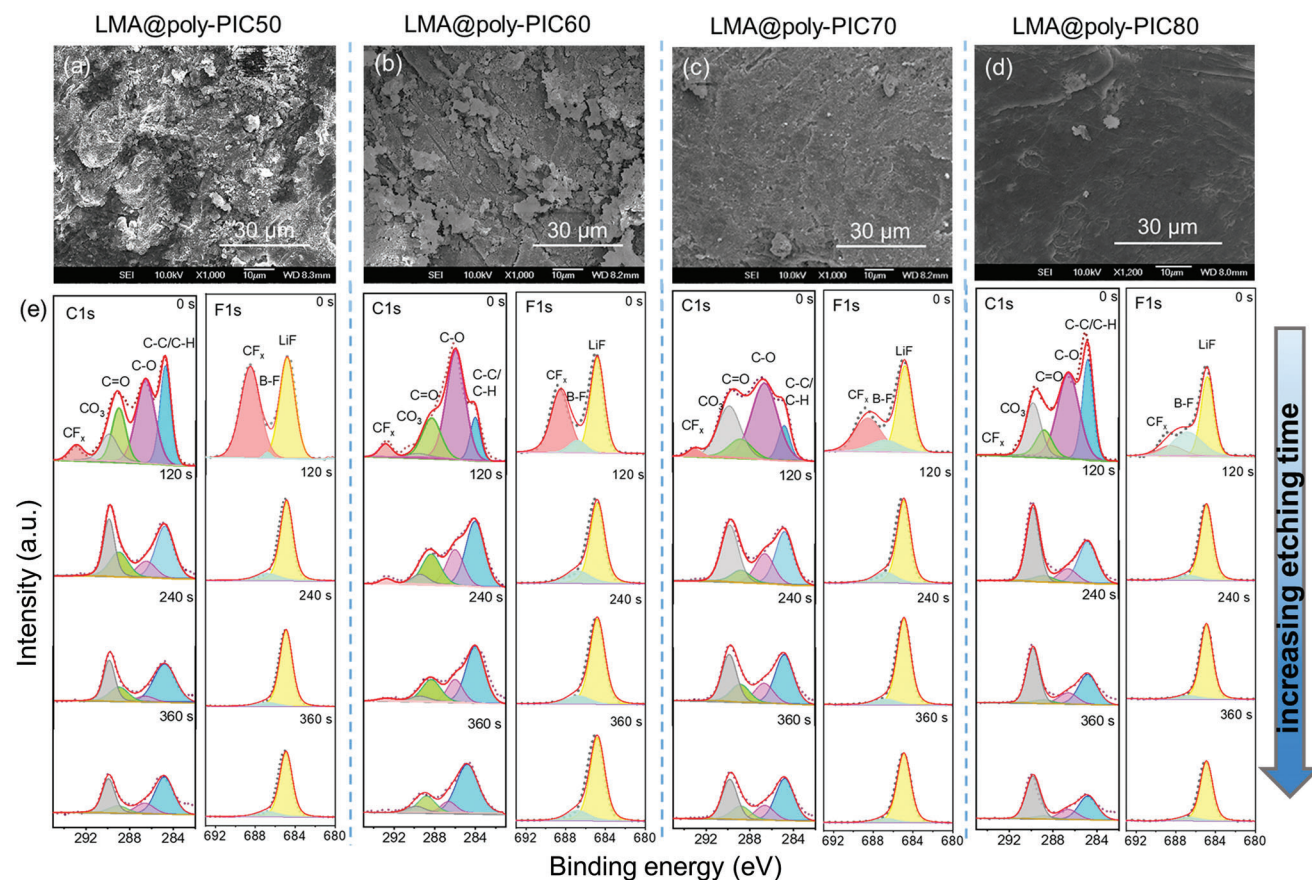


Figure 5. SEM images of the surface of LMAs from the cycled (50 cycles) Li/LFP batteries with a) poly-PIC50, b) poly-PIC60, c) poly-PIC70, and d) poly-PIC80 electrolytes. e) C 1s and F 1s spectra of the LMAs from the cycled Li/LFP batteries with poly-PIC50, poly-PIC60, poly-PIC70, and poly-PIC80.

3. Conclusion

We successfully developed a class of LLZTO-based polymer-ceramic composite electrolytes for use in solid-state Li-metal batteries. These electrolytes exhibit high ionic conductivity, wide electrochemical windows, and strong mechanical properties. Among the electrolytes synthesized, poly-PIC80 was found to be particularly promising, exhibiting high ionic conductivity at various temperatures, a high Li^+ transference number, and a high Young's modulus. When tested in Li symmetric and asymmetric Li/Cu cells, poly-PIC80 demonstrated excellent cycling stability at room temperature. In addition, the use of poly-PIC80 in a Li/LFP battery led to a high specific capacity over 500 cycles. Moreover, when matched with a high-voltage NMC811 cathode, poly-PIC80-based Li-metal batteries maintained a discharge capacity of 140 mAh g^{-1} over 80 cycles at 23°C . Our experimental and computational analyses also provide insight into the mechanisms behind the formation and composition of the solid-electrolyte interphase, which contributes to the enhanced capacity and stability of these batteries. These findings represent a significant advance toward the development of high-energy-density and high-safety solid-state Li-metal batteries that can be utilized at room temperature.

4. Experimental Section

Materials: $\text{LiOH} \cdot \text{H}_2\text{O}$ ($\geq 99.0\%$, Sigma-Aldrich), ZrO_2 ($< 100 \text{ nm}$, Sigma-Aldrich), Ta_2O_5 ($\geq 99\%$, Alfa Aesar), LiTFSI (99%, Sigma-Aldrich), LiBOB (98%, Dkmchem), LiPF_6 (99%, Sigma-Aldrich), polyvinylidene fluoride (PVDF, Solef 5130, Solvay), DOL (AR, Dieckmann), N, N-dimethylformamide (DMF, 99.9%, Prolabo), methyl propionate (MP, 99%, Aladdin), fluoroethylene carbonate (FEC, 98%, Alfa Aesar), N-methyl-2-pyrrolidone (NMP, 99.9%, MTI), Carbon black (TIMICAL SUPER C65, MTI), LFP (Aleees), and NMC811 (Shanshan Corporation) were used without further treatment. La_2O_3 (99%, Sigma-Aldrich) was dried at 900°C for 12 h to remove H_2O .

Preparation of LLZTO: LLZTO was fabricated by a solid-state reaction method in the previous work.^[6b,23] Stoichiometric amounts of La_2O_3 , $\text{LiOH} \cdot \text{H}_2\text{O}$, ZrO_2 , and Ta_2O_5 were mixed in isopropanol and ball milled thoroughly. After drying at 200°C on a hot plate for 2 h, the precursor powder was calcined at 900°C for 12 h in a MgO crucible. After adding an extra 10 wt.% $\text{LiOH} \cdot \text{H}_2\text{O}$ and 0.3 wt.% Al_2O_3 , the sintered powder was ground and uniaxially pressed into pellets. The obtained pellets were kept at 1140°C for 16 h to synthesize LLZTO. Lastly, the pellets were ground again for 24 h at 500 rpm in a ball miller and stored in an Ar-filled glovebox ($[\text{H}_2\text{O}] < 0.01 \text{ ppm}$, $[\text{O}_2] < 0.01 \text{ ppm}$, Super 1220/750, Mikrouna).

Preparation of Electrolytes: 0.172 g LiTFSI, 0.078 g LiBOB, and $(1-x)$ g PVDF ($x = 0.5, 0.6, 0.7, \text{ or } 0.8$) were first stirred into 6.0 mL DMF at 60°C to obtain a transparent solution. Then, x g of LLZTO powder was added to the solution that was further stirred at 60°C for 12 h. The viscous

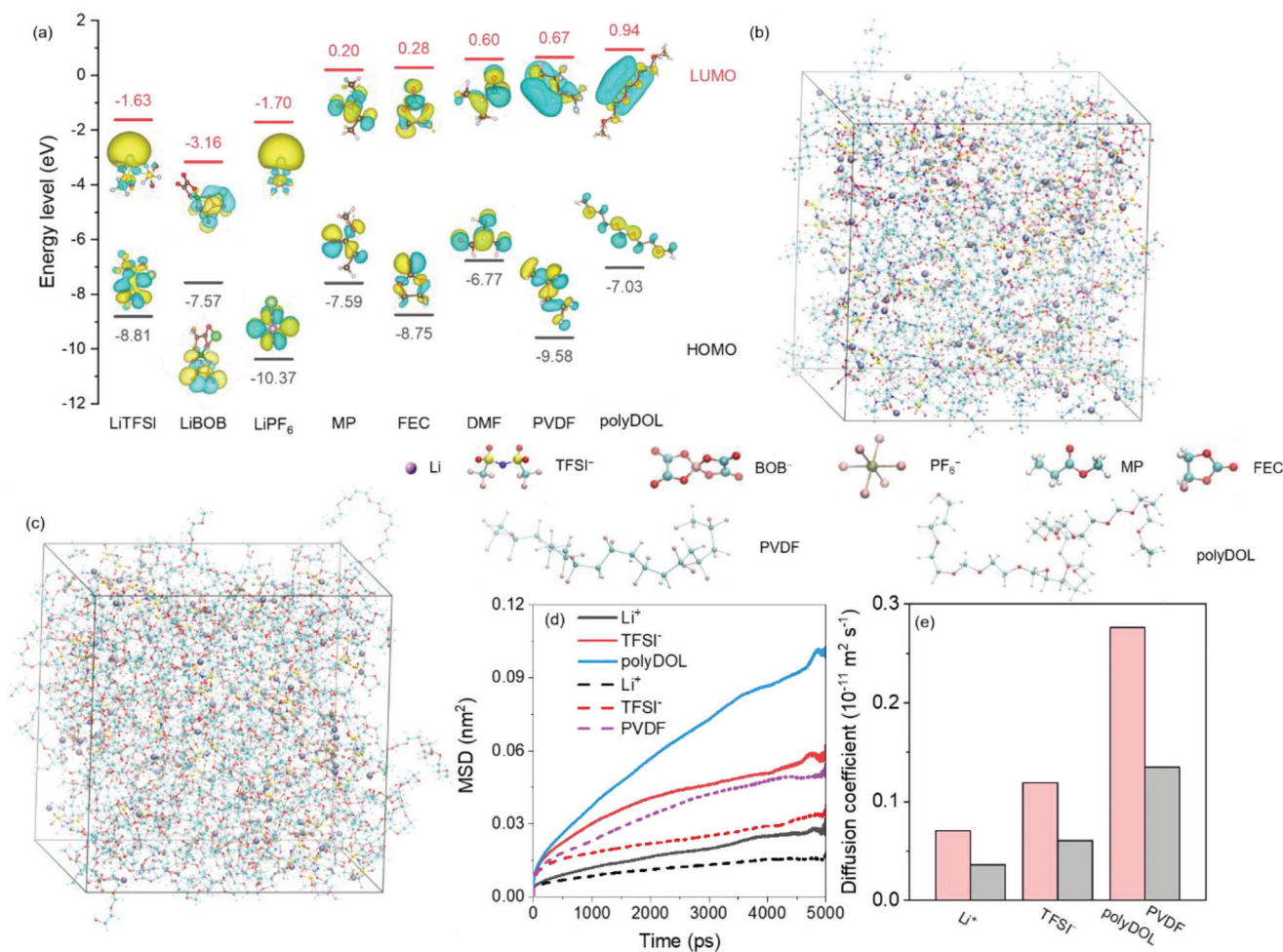


Figure 6. a) LUMO and HOMO of the poly-PIC components. Snapshots of the MD simulation of the b) PVDF- and c) polyDOL-based polymer electrolytes. d) MSD versus time for the PVDF-based polymer electrolyte (dotted line) and polyDOL-based polymer electrolyte (solid line). e) Corresponding diffusion coefficients of the PVDF-based polymer electrolyte (grey) and the polyDOL-based polymer electrolyte (pink).

mixture was then cast on a glass dish and dried for 8 h in a vacuum oven at 60 °C to obtain the PVDF/LLZTO membrane. Based on the LLZTO mass, x , the membrane was denoted as polyDOL-free-PICX, where $X = 100x$. For the preparation of polyDOL, 0.144 g LiTFSI, 300.0 μ L DOL, and 50.0 μ L FEC were first mixed into a vial. Then, 0.038 g LiPF₆ previously dissolved into 150.0 μ L of MP was also added to the vial to further obtain the polyDOL precursor solution. Finally, 25.0 μ L of the solution was immediately injected into polyDOL-free-PICX. The polyDOL-enhanced PIC was denoted as poly-PICX ($X = 100x$). The thickness of poly-PICX was controlled in the range of 100–110 μ m. The PVDF membrane without LLZTO was also prepared by tape casting; 0.172 g of LiTFSI, 0.078 g of LiBOB, and 0.5 g of PVDF were added into 6.0 mL of DMF and stirred at 60 °C for 12 h to obtain a viscous solution. Subsequently, the solution was cast on a glass dish and dried for 8 h in a vacuum oven at 60 °C to obtain the PVDF membrane.

Cathode Preparation: LFP, conductive carbon black, and PVDF were combined in the NMP solvent with a weight ratio of 8:1:1 and magnetically stirred on a hot plate for 12 h. The obtained slurry was then cast onto an Al foil and dried at 90 °C for 8 h to produce an electrode. In general, the mass loading of the LFP cathode was in the 2.5–3.0 mg cm⁻² range. In addition, LFP and NMC811 electrodes with a higher mass loading of 7.9 and 6.9 mg cm⁻², respectively, were prepared using a similar process, which involved mixing the active material, carbon black, and PVDF in a weight ratio of 9:0.6:0.4.

Physical Characterizations: FTIR characterization was performed using a Bruker Vertex 70 FTIR spectrometer. SEM (JEOL-6700F and JEOL-6390) was used to document the morphology of the LLZTO particles, poly-PICs, and Li metal surfaces after cycling. A zeta potential nano-particle analyzer (ZetaPlus) was employed to determine the size distribution of LLZTO particles. To test the wettability between the polyDOL precursor and the PP, PVDF, and PVDF/LLZTO (e.g., polyDOL-free-PIC80), contact angle measurements were conducted using a contact angle instrument (SDC-100, SINDIN). TGA (SA Q5000, TA instrument) was performed from room temperature to 750 °C at a heating rate of 10 °C min⁻¹ under N₂ flow. XRD (PANalytical Empyrean Pro diffractometer) was conducted with Cu K α radiation ($\lambda = 1.5406$ Å) in the 2θ range from 10 to 70°. Tensile tests were conducted using a UTM-12 universal testing machine at a crosshead speed of 10 mm min⁻¹. XPS was recorded using a PHI5600 X-ray photoelectron spectrometer. The cycled Li metal anodes were washed three times with dimethyl carbonate (DMC) prior to XPS characterization.

Electrochemical Characterizations: All cells characterized electrochemically were assembled within a glovebox (MIKOUNA). The ionic conductivity (σ) of poly-PICs was calculated by $\sigma = \frac{L}{RA}$, where A is the contact area between poly-PIC and SS, L is the thickness of poly-PIC, R is the measured ohmic resistance of a SS|poly-PIC|SS (SS = stainless steel) symmetric cell that can be obtained from the electrochemical impedance spectroscopy (EIS) spectra. EIS was measured within the frequency range of 0.5 Hz to

7 MHz using a Bio-Logic VSP-300 electrochemical workstation. The activation energy (E_a) was obtained following the Arrhenius equation $\sigma(T) = Ae^{-\frac{E_a}{k_B T}}$, where T is the measurement temperature, A is a pre-exponential factor, and k_B is the Boltzmann constant. The temperature-dependent conductivity tests were performed in a thermal chamber (SU-242-5, ESPEC North America). The t_{Li^+} was calculated using the formula $t_{Li^+} = \frac{I_{ss}(\Delta V - I_0 R_0)}{I_0(\Delta V - I_{ss} R_{ss})}$, where the I_0 and I_{ss} are the initial and steady-state currents obtained by chronoamperometry, ΔV is the DC voltage applied, which is 10.0 mV, and R_0 and R_{ss} are the initial and steady state resistances observed from EIS. Linear sweep voltammetry (potential range of 2–6 V at a scan rate of 5 mV s⁻¹) was used to determine the oxidation potential, using a Li|poly-PIC|SS cell. Cycling of symmetric cells and full batteries were performed using a CT2001A battery testing system (LANHE). Li|poly-PIC|LFP and Li|poly-PIC|NMC811 batteries were cycled within the voltage range of 2.5–4.2 and 2.8–4.3 V, respectively.

Density Functional Theory Calculations: DFT calculations were carried out in Gaussian 09^[31] with a hybrid B3LYP functional^[32] and 6-311G(d,p) basis set^[33]. The molecular structures of different electrolyte components were first optimized until forces converged within 4.5×10^{-4} Hartrees Bohr⁻¹. Next, the energy of molecular orbitals was obtained using the optimal molecular structures. HOMO and LUMO were visualized with GaussView 5.0.9.^[34]

Molecular Dynamics Simulations: Classical MD simulations were carried out with GROMACS^[35]. The OPLS-AA force field^[36] and restrained electrostatic potential (RESP) charge (obtained using Multiwfn^[37]) were used. Bonds with hydrogen atoms were constrained using the linear constraint solver (LINCS) algorithm^[38]. In the case of the polyDOL-free-PIC electrolyte, 60 LiTFSI, 40 LiBOB, 237 DMF, and 31 PVDF (degree of polymerization was set at ten) were added to a $300 \times 300 \times 300 \text{ \AA}^3$ box. In the case of the poly-PIC electrolyte, 47 LiTFSI, 23 LiPF₆, 215 MP, 62 FEC, and 40 polyDOL (degree of polymerization was set at ten) were added to a $300 \times 300 \times 300 \text{ \AA}^3$ box. First, the model system was relaxed for 100 ps under a canonical ensemble (NVT). Then, it was equilibrated for 5 ns (time step = 1 fs) under an isothermal–isobaric (NPT) ensemble. After equilibration, the box shrank to $80 \times 80 \times 80 \text{ \AA}^3$, and the system reached a density of 1.57 g cm⁻³. After that, a simulation lasting 5 ns (time step = 1 fs) was carried out under the NVT ensemble. The temperature for NPT equilibration and NVT production was controlled at 296.15 K using Nosé–Hoover temperature coupling. The pressure for NPT equilibration was controlled at 1 bar using Parrinello–Rahman pressure coupling (coupling constant = 2 ps). Particle-Mesh-Ewald (PME) method^[39] (cut-off distance = 1.0 nm) was used to handle electrostatic interactions. The simulation results were visualized using VMD.^[40]

The RDF of a solvent or anion was calculated using $g(r) = \frac{n_r}{4\pi r^2 \rho \Delta r}$, where r is the distance of an atom from the reference atom, ρ is the average probability density of an atom type in the system, and n_r is the number of atoms of the given species within a shell of radius r and a thickness of Δr . Therefore, the $g(r)$ was averaged over the entire simulation time.

The MSD of a certain species was calculated using $MSD(t) = \frac{1}{N} \sum_{i=1}^N |r_i(t) - r_i(0)|^2$, where $r_i(0)$ and $r_i(t)$ are the initial (time = 0) and final (time = t) positions of the i th particle of that species, respectively (N = total number of particles of that species). Correspondingly, the self-diffusion coefficient, D , of that species was obtained from the following formula: $D = \lim_{\Delta t \rightarrow \infty} \frac{MSD(t_0 + \Delta t) - MSD(t_0)}{6\Delta t}$, where t_0 = initial time.^[41]

Supporting Information

Supporting Information is available from the Wiley Online Library or from the author.

Acknowledgements

Y.J. and G.Z. contributed equally to this work. The authors acknowledge the support from the Research Grants Council of Hong Kong (16206019

and 16201820) and the Hetao Shenzhen-Hong Kong Science and Technology Innovation Cooperation Zone (HZQB-KCZYB-2020083). The authors also thank HKUST Fok Ying Tung Research Institute and National Supercomputing Center in Guangzhou Nansha sub-center for providing high-performance computational resources.

Open access funding enabled and organized by Projekt DEAL.

Conflict of Interest

The authors declare no conflict of interest.

Data Availability Statement

The data that support the findings of this study are available from the corresponding author upon reasonable request.

Keywords

in situ formations, Li-metal batteries, low interfacial resistivities, polymer-in-ceramic, solid-state batteries

Received: May 10, 2023
Published online: June 6, 2023

- a) J. Holoubek, H. Liu, Z. Wu, Y. Yin, X. Xing, G. Cai, S. Yu, H. Zhou, T. A. Pascal, Z. Chen, P. Liu, *Nat. Energy* **2021**, *6*, 303; b) J. Liu, Z. Bao, Y. Cui, E. J. Dufek, J. B. Goodenough, P. Khalifah, Q. Li, B. Y. Liaw, P. Liu, A. Manthiram, Y. S. Meng, V. R. Subramanian, M. F. Toney, V. V. Viswanathan, M. S. Whittingham, J. Xiao, W. Xu, J. Yang, X.-Q. Yang, J.-G. Zhang, *Nat. Energy* **2019**, *4*, 180; c) Y. Zhang, T.-T. Zuo, J. Popovic, K. Lim, Y.-X. Yin, J. Maier, Y.-G. Guo, *Mater. Today* **2020**, *33*, 56; d) J. Janek, W. G. Zeier, *Nat. Energy* **2016**, *1*, 16141; e) J. Wu, X. Chen, W. Fan, X. Li, Y.-W. Mai, Y. Chen, *Energy Storage Mater.* **2022**, *48*, 223.
- a) C. Yang, K. Fu, Y. Zhang, E. Hitz, L. Hu, *Adv. Mater.* **2017**, *29*, 1701169; b) J. M. Tarascon, M. Armand, *Nature* **2001**, *414*, 359.
- X.-B. Cheng, R. Zhang, C.-Z. Zhao, Q. Zhang, *Chem. Rev.* **2017**, *117*, 10403.
- a) X.-B. Cheng, C.-Z. Zhao, Y.-X. Yao, H. Liu, Q. Zhang, *Chem* **2019**, *5*, 74; b) L.-Z. Fan, H. He, C.-W. Nan, *Nat. Rev. Mater.* **2021**, *6*, 1003.
- a) Y. Ren, K. Chen, R. Chen, T. Liu, Y. Zhang, C.-W. Nan, *J. Am. Ceram. Soc.* **2015**, *98*, 3603; b) D. Lin, W. Liu, Y. Liu, H. R. Lee, P.-C. Hsu, K. Liu, Y. Cui, *Nano Lett.* **2016**, *16*, 459; c) S. Choudhury, R. Mangal, A. Agrawal, L. A. Archer, *Nat. Commun.* **2015**, *6*, 10101; d) Y. Tominaga, K. Yamazaki, *Chem. Commun.* **2014**, *50*, 4448; e) K. Pan, L. Zhang, W. Qian, X. Wu, K. Dong, H. Zhang, S. Zhang, *Adv. Mater.* **2020**, *32*, 2000399.
- a) L. Chen, Y. Li, S.-P. Li, L.-Z. Fan, C.-W. Nan, J. B. Goodenough, *Nano Energy* **2018**, *46*, 176; b) J. Yu, Y.-Q. Lyu, J. Liu, M. B. Effat, S. C. T. Kwok, J. Wu, F. Ciucci, *J. Mater. Chem. A* **2019**, *7*, 17995; c) W. Zhang, J. Nie, F. Li, Z. L. Wang, C. Sun, *Nano Energy* **2018**, *45*, 413; d) X. Zhang, B.-Q. Xu, Y.-H. Lin, Y. Shen, L. Li, C.-W. Nan, *Solid State Ionics* **2018**, *327*, 32.
- F. Croce, G. B. Appetecchi, L. Persi, B. Scrosati, *Nature* **1998**, *394*, 456.
- a) C. Yan, P. Zhu, H. Jia, Z. Du, J. Zhu, R. Orenstein, H. Cheng, N. Wu, M. Dirican, X. Zhang, *Energy Storage Mater.* **2020**, *26*, 448; b) J. Bae, Y. Li, J. Zhang, X. Zhou, F. Zhao, Y. Shi, J. B. Goodenough, G. Yu, *Angew. Chem., Int. Ed.* **2018**, *57*, 2096.

- [9] W.-P. Chen, H. Duan, J.-L. Shi, Y. Qian, J. Wan, X.-D. Zhang, H. Sheng, B. Guan, R. Wen, Y.-X. Yin, S. Xin, Y.-G. Guo, L.-J. Wan, *J. Am. Chem. Soc.* **2021**, *143*, 5717.
- [10] J. Zheng, M. Tang, Y.-Y. Hu, *Angew. Chem., Int. Ed.* **2016**, *55*, 12538.
- [11] a) X. Yu, A. Manthiram, *Energy Storage Mater.* **2021**, *34*, 282; b) S. Li, S.-Q. Zhang, L. Shen, Q. Liu, J.-B. Ma, W. Lv, Y.-B. He, Q.-H. Yang, *Adv. Sci.* **2020**, *7*, 1903088.
- [12] Y.-C. Jung, S.-M. Lee, J.-H. Choi, S. S. Jang, D.-W. Kim, *J. Electrochem. Soc.* **2015**, *162*, A704.
- [13] a) H. Huo, Y. Chen, J. Luo, X. Yang, X. Guo, X. Sun, *Adv. Energy Mater.* **2019**, *9*, 1804004; b) J. Zhang, N. Zhao, M. Zhang, Y. Li, P. K. Chu, X. Guo, Z. Di, X. Wang, H. Li, *Nano Energy* **2016**, *28*, 447.
- [14] A. Li, X. Liao, H. Zhang, L. Shi, P. Wang, Q. Cheng, J. Borovilas, Z. Li, W. Huang, Z. Fu, M. Dontigny, K. Zaghib, K. Myers, X. Chuan, X. Chen, Y. Yang, *Adv. Mater.* **2020**, *32*, 1905517.
- [15] J. Pan, P. Zhao, N. Wang, F. Huang, S. Dou, *Energy Environ. Sci.* **2022**, *15*, 2753.
- [16] R. Chen, W. Qu, X. Guo, L. Li, F. Wu, *Mater. Horiz.* **2016**, *3*, 487.
- [17] K. M. Diederichsen, E. J. McShane, B. D. McCloskey, *ACS Energy Lett.* **2017**, *2*, 2563.
- [18] Y. He, C. Lu, S. Liu, W. Zheng, J. Luo, *Adv. Energy Mater.* **2019**, *9*, 1901810.
- [19] L. Xu, S. Tang, Y. Cheng, K. Wang, J. Liang, C. Liu, Y.-C. Cao, F. Wei, L. Mai, *Joule* **2018**, *2*, 1991.
- [20] a) Q. Zhao, X. Liu, S. Stalin, K. Khan, L. A. Archer, *Nat. Energy* **2019**, *4*, 365; b) V. Vijayakumar, B. Anothumakkool, S. Kurungot, M. Winter, J. R. Nair, *Energy Environ. Sci.* **2021**, *14*, 2708; c) T. Liu, J. Zhang, W. Han, J. Zhang, G. Ding, S. Dong, G. Cui, *J. Electrochem. Soc.* **2020**, *167*, 070527.
- [21] J. Yu, J. Liu, X. Lin, H. M. Law, G. Zhou, S. C. T. Kwok, M. J. Robson, J. Wu, F. Ciucci, *Energy Storage Mater.* **2021**, *37*, 609.
- [22] a) J. Yu, X. Lin, J. Liu, J. T. T. Yu, M. J. Robson, G. Zhou, H. M. Law, H. Wang, B. Z. Tang, F. Ciucci, *Adv. Energy Mater.* **2022**, *12*, 2102932; b) J. Xiang, Y. Zhang, B. Zhang, L. Yuan, X. Liu, Z. Cheng, Y. Yang, X. Zhang, Z. Li, Y. Shen, J. Jiang, Y. Huang, *Energy Environ. Sci.* **2021**, *14*, 3510.
- [23] J. Yu, S. C. T. Kwok, Z. Lu, M. B. Effat, Y.-Q. Lyu, M. M. F. Yuen, F. Ciucci, *ChemElectroChem* **2018**, *5*, 2873.
- [24] a) X. Zhang, T. Liu, S. Zhang, X. Huang, B. Xu, Y. Lin, B. Xu, L. Li, C.-W. Nan, Y. Shen, *J. Am. Chem. Soc.* **2017**, *139*, 13779; b) J. Sastre, A. Priebe, M. Döbeli, J. Michler, A. N. Tiwari, Y. E. Romanyuk, *Adv. Mater. Interfaces* **2020**, *7*, 2000425.
- [25] Z. Lu, J. Yu, J. Wu, M. B. Effat, S. C. T. Kwok, Y. Lyu, M. M. F. Yuen, F. Ciucci, *Energy Storage Mater.* **2019**, *18*, 311.
- [26] a) B. Zhang, Y. Liu, J. Liu, L. Sun, L. Cong, F. Fu, A. Mauger, C. M. Julien, H. Xie, X. Pan, *J. Energy Chem.* **2021**, *52*, 318; b) F. P. Nkosi, M. Valvo, J. Mindemark, N. A. Dzulurnain, G. Hernández, A. Mahun, S. Abbrent, J. Brus, L. Kobera, K. Edström, *ACS Appl. Energy Mater.* **2021**, *4*, 2531.
- [27] Y. Zhao, L. Wang, Y. Zhou, Z. Liang, N. Tavajohi, B. Li, T. Li, *Adv. Sci.* **2021**, *8*, 2003675.
- [28] L. Chen, W. Li, L.-Z. Fan, C.-W. Nan, Q. Zhang, *Adv. Funct. Mater.* **2019**, *29*, 1901047.
- [29] J. Zheng, M. H. Engelhard, D. Mei, S. Jiao, B. J. Polzin, J.-G. Zhang, W. Xu, *Nat. Energy* **2017**, *2*, 17012.
- [30] X. Dong, Y. Lin, P. Li, Y. Ma, J. Huang, D. Bin, Y. Wang, Y. Qi, Y. Xia, *Angew. Chem., Int. Ed.* **2019**, *58*, 5623.
- [31] M. J. Frisch, G. W. Trucks, H. B. Schlegel, G. E. Scuseria, M. A. Robb, J. R. Cheeseman, G. Scalmani, V. Barone, G. A. Petersson, H. Nakatsuji, X. Li, M. Caricato, A. Marenich, J. Bloino, B. G. Janesko, R. Gomperts, B. Mennucci, H. P. Hratchian, J. V. Ortiz, A. F. Izmaylov, J. L. Sonnenberg, D. Williams-Young, F. Ding, F. Lipparini, F. Egidi, J. Goings, B. Peng, A. Petrone, T. Henderson, D. Ranasinghe, et al., Gaussian, Inc., Wallingford CT, **2016**.
- [32] A. D. Becke, *J. Chem. Phys.* **1993**, *98*, 5648.
- [33] a) R. Krishnan, J. S. Binkley, R. Seeger, J. A. Pople, *J. Chem. Phys.* **1980**, *72*, 650; b) M. J. Frisch, J. A. Pople, J. S. Binkley, *J. Chem. Phys.* **1984**, *80*, 3265.
- [34] R. Dennington, T. Keith, J. Millam, GaussView, Version 5.0.8.: Semichem Inc., Shawnee Mission KS; **2009**.
- [35] M. J. Abraham, T. Murtola, R. Schulz, S. Páll, J. C. Smith, B. Hess, E. Lindahl, *SoftwareX* **2015**, *1-2*, 19.
- [36] W. L. Jorgensen, D. S. Maxwell, J. Tirado-Rives, *J. Am. Chem. Soc.* **1996**, *118*, 11225.
- [37] a) T. Lu, F. Chen, *J. Comput. Chem.* **2012**, *33*, 580; b) C. F.-W. Lu Tian, *Acta Phys.-Chim. Sin.* **2012**, *28*, 1.
- [38] a) B. Hess, H. Bekker, H. J. C. Berendsen, J. G. E. M. Fraaije, *J. Comput. Chem.* **1997**, *18*, 1463; b) B. Hess, *J. Chem. Theory Comput.* **2008**, *4*, 116.
- [39] a) T. Darden, D. York, L. Pedersen, *J. Chem. Phys.* **1993**, *98*, 10089; b) U. Essmann, L. Perera, M. L. Berkowitz, T. Darden, H. Lee, L. G. Pedersen, *J. Chem. Phys.* **1995**, *103*, 8577.
- [40] W. Humphrey, A. Dalke, K. Schulten, *J. Mol. Graphics* **1996**, *14*, 33.
- [41] A. Einstein, *Ann. Phys.* **1905**, *4*, 549.